PAPER

Photocatalytic activity of micron-scale brass on emerging pollutant degradation in water: mechanism elucidation and removal efficacy assessment†

Irwing M. Ramirez-Sanchez,[a] Onur G. Apul [b] and Navid B. Saleh [*a]

Alloys or smelted metal mixtures have served as cornerstones of human civilization. The advent of smelted copper and tin, *i.e.*, bronze, in the 4th millennium B.C. in Mesopotamia has pioneered the preparation of other metal composites, such as brass (*i.e.*, mixture of copper and zinc), since the bronze age. The contemporary use of these alloys has expanded beyond using their physical strength. The catalytic chemistry of micron-scale brass or copper–zinc alloy can be utilized to effectively degrade emerging contaminants (ECs) in water, which are presenting significant risks to human health and wildlife. Here, we examine the photocatalytic activity of a commercially available micro-copper–zinc alloy (KDF® 55, MicroCuZn), made with earth abundant metals, for oxidative removal of two ECs. The micron-scale brass is independently characterized for its morphology, which confirms that it has the β-brass phase and that its plasmonic response is around 475 nm. Estriol (E3), a well-known EC, is removed from water with ultraviolet (UV) radiation catalyzed by MicroCuZn and H_2O_2–MicroCuZn combinations. The synergy between H_2O_2, UV, and MicroCuZn enhances hydroxyl radical (˙OH) generation and exhibit a strong pseudo-first-order kinetic degradation of E3 with a decay constant of 1.853×10^{-3} min^{-1} ($r^2 = 0.999$). Generation of ˙OH is monitored with *N,N*-dimethyl-4-nitrosoaniline (*p*NDA) and terephthalic acid (TA), which are effective ˙OH scavengers. X-ray photoelectron spectroscopy analysis has confirmed ZnO/CuO–Cu_2O film formation after UV irradiation. The second EC studied here is Δ9-tetrahydrocannabinol or THC, a psychotropic compound commonly consumed through recreational or medicinal use of marijuana. The exceptionally high solids–water partitioning propensity of THC makes adsorption the dominant removal mechanism, with photocatalysis potentially supporting the removal efficacy of this compound. These results indicate that MicroCuZn can be a promising oxidative catalyst especially for degradation of ECs, with possible reusability of this historically significant material with environmentally-friendly attributes.

1. Introduction

Being present in trace amounts, pharmaceuticals, hormones, and personal care products manifest new challenges for water treatment.[1] Although water treatment technologies are continuing to be developed for effective removal and degradation of a wide variety of Emerging Contaminants (ECs),[2] some crucial challenges in these efforts have been identified, which include: high energy consumption, excess chemical inputs, large carbon and physical footprint, increased cost, and lack of reusability.[3] There is a critical need for developing smart

materials, which can be prepared with earth-abundant resources, to effectively remove ECs from water. One such material that has promise to overcome some of these limitations is brass, a bimetallic alloy made with copper (55–90%) and zinc (10–45%). Brass, a historically significant material that was invented in the bronze age and has served as one of the cornerstones of human civilization, also demonstrated unique advantages in environmental applications; *e.g.*, as biocidal agents[4] and in biofuel conversion,[5] CO_2 reduction,[6] air pollution control,[7] and water treatment.[8,9]

One of the cost-effective (average cost of USD 0.019 g^{-1}) micron-scale brass is KDF® 55 (hereafter MicroCuZn), which has become popular in water treatment.[10–15] MicroCuZn has extensively been applied in filters to remove manganese,[16] chlorine,[11] mercury,[10,13] antimony(III),[17] chromium(VI),[12] copper(II),[18] and silver nanoparticles.[15] It has been suggested that the removal mechanism of heavy metals by MicroCuZn is *via*

[a]*Department of Civil, Architectural and Environmental Engineering, The University of Texas at Austin, Austin, TX, 78712, USA. E-mail: navid.saleh@utexas.edu; Tel: +1 512 471 9175*

[b]*Civil and Environmental Engineering, University of Maine, Orono, ME 04469, USA*

† Electronic supplementary information (ESI) available. See DOI: 10.1039/d0ra06153k

reduction of the metal and subsequent formation of amalgams.[10] Even though MicroCuZn has been predominantly used for removal of inorganic ions, its efficacy for organic contaminant degradation has hardly been assessed; evaluation of its promise for the same is imperative.

The rationale for using MicroCuZn as an oxidative catalyst for organic degradation emanates from previous reports, where copper foil activated by ozone removed organic pollutants with hydroxyl radical ($^\bullet$OH) attack.[19] Similarly, when brass is exposed to hydrogen peroxide (H_2O_2),[20] a common oxidant, or to photoradiation,[21,22] it can modulate reactive oxygen species (ROS) generation. H_2O_2 has also been shown to initiate corrosion by electroreduction.[20] Besides, it has been confirmed that Cu, upon exposure to ultraviolet radiation (UV), forms a stable oxide film.[23–25] The photo-corrosion could be brought about by the photo-induced holes (h^+) that transport across the crystals within brass, accelerating the cathodic reactions.[22]

Emerging pharmaceuticals, particularly Δ9-tetrahydrocannabinol (THC) and estriol (E3), are structurally similar with the presence of a phenol moiety and with their relatively high octanol–water partition coefficients values, i.e., $10^{6.97}$ and $10^{2.45}$, respectively; were chosen as model contaminants. THC, the primary chemical compound in marijuana, is a psychotropic substance that belongs to the cannabinoid family.[26–28] THC and similar cannabis molecules and their metabolites are suspected of transforming into toxic disinfection byproducts (DBPs) during their passage through the treatment systems.[26,28] Similarly, E3 is released into the aquatic environment in notable amounts for their use in hormone replacement therapy,[29] and is known to present severe risks to the environment and humans.[30] An oxidative transformation of these pharmaceuticals can potentially break open the phenolic structures and reduce potential halogenation during their passage through the treatment systems. Ring-opening and chain-shortening reactions achieved using a potent oxidant can present with a promising route to avoid DBP generation.

The objective of this study is to elucidate the catalytic and photocatalytic mechanisms of a commercially available micronscale brass to remove the two model ECs (with unique molecular structure and covering for a wide range of solids–water partition coefficient) from water. In particular, the catalytic mechanisms are examined with combinations of MicroCuZn and H_2O_2, with and without UV irradiation. Oxidative catalytic rate is measured, followed by elucidation of underlying mechanism with monitoring of $^\bullet$OH with N,N-dimethyl-p-nitrosoaniline (pNDA), and terephthalic acid (TA). To evaluate the efficacy of the material beyond its oxidative performance, reusability and stability are also examined.

2. Experimental

2.1. Materials

pNDA (97%), E3 (≥97%), TA (98%), and 2-hydroxyterephthalic acid (2-THA, 97%) were procured from Sigma-Aldrich (St. Louis, MO, USA). THC (97%) in methanol was obtained from Restek (Bellefonte, PA, USA). H_2O_2 (30%) was procured from J. T. Baker (Phillipsburg, NJ, USA). HPLC grade acetonitrile (99.99%) was purchased from Fisher Scientific (Fair Lawn, NJ, USA). All solutions and HPLC mobile phases were prepared with ultrapure water (Millipore, Burlington, MA, USA). These chemicals were reagent grade and used with no further purification.

KDF® 55 (MicroCuZn) was procured from KDF Fluid Treatment Inc. (Three Rivers, MI, USA). Fig. S1† shows MicroCuZn material, as used in this study. The MicroCuZn was ultrasonically washed with acetone, ethanol, and deionized (DI) water for 10 min each, and then dried at 90 °C for 6 h.

2.2. Material characterization

Surface morphology was examined with scanning electron microscopy (SEM) using a FEI Quanta FEG 650 SEM (FEI Company, Hillsboro, OR, USA), equipped with an energy dispersive X-ray spectroscopy (EDS) attachment (Bruker, Madison, WI, USA). Ferret's diameter, projected area, and circularity distributions were obtained from SEM images for 48 grains, chosen randomly. Transmission electron microscopy (TEM) images were collected with a JEOL 2010F TEM (Japan Electronics Co. Ltd, Tokyo, Japan). SEM and TEM images were analyzed with ImageJ (NIH, Bethesda, ML). X-ray diffraction (XRD) analysis was conducted on R-Axis Spider (Rigaku Corporation, Japan) diffractometer. The phase identification was conducted with QualX2.0 software, developed by Altomare et al.[31] Nitrogen adsorption isotherms were generated at 77.4 K, with a Quantachrome Autosorb-1 gas adsorption analyzer to determine specific Brunauer–Emmett–Teller (BET) surface area (Quantachrome Instruments, Boynton Beach, FL, USA). Prior to analysis, the samples were outgassed at 293.15 K for 40 h. Diffused reflectance measurement was obtained by forming pellets and conducting measurements on a Lambda 365 UV-vis spectrophotometer (PerkinElmer, Waltham, MA, USA) with $BaSO_4$ as the reference. X-ray photoelectron spectroscopy (XPS) was conducted with a Kratos AXIS Ultra DLD (Shimadzu Corporation, Japan), equipped with a monochromatic Al Kα (1486.6 eV) X-ray source. The C 1s peak at binding energy of 284.5 eV was used as an energy reference. XPS spectrum for Cu $2p_{3/2}$ region was deconvoluted into four components; i.e., copper metal (Cu(0)), cuprous oxide (Cu_2O), cupric oxide (CuO) and copper hydroxide ($Cu(OH)_2$) with regard to binding energy values reported earlier.[32] The Zn-region was deconvoluted for Zn $2p_{3/2}$, taking into account two components; i.e., zinc metal (Zn(0)) and zinc oxide (ZnO), based on binding energies that have been extensively reported.[33] The XPS spectra were fitted with XPS peak 4.1 software, following Raymund W. M. Kwok (The Chinese University of Hong Kong, China), with a 80 : 20 Gaussian–Lorenzian mixed-function having the Shirley background correction.

2.3. Batch photocatalytic conditions

The photoreactor was constructed with a 100 mL cylindrical water-cooled, jacketed glass vessel (Fig. S2a†), placed on a thermostatic bath (F250 Julabo, Seelbach, Germany) that maintained 20 °C for all experiments. To ensure that THC adsorption to the reactor wall does not interfere with the photocatalytic degradation assessment, future studies should explore reactor materials (such as silanized glass) with

minimum THC sorption propensity. The initial concentrations of E3, THC, *p*NDA, and TA were 10, 1, 10 and 500 μM, respectively. All experiments were adjusted to pH 7.0 with 10 mM NaOH solutions, except for the TA solutions (*i.e.*, pH 9.0) to ensure adequate TA solubility.[34] pH 7.0 was selected because of copper's thermodynamic instability in deionized H_2O (with dissolved oxygen) at pH below 7.0 according to the Pourbaix diagram for copper at 25 °C.[35] Future studies may consider examining photocatalytic behavior of brass in alkaline media.

The system was set in an enclosed wooden box to avoid interference from ambient light (Fig. S2b†). The catalyst load was maintained at 10 g L^{-1}. A high catalyst load was chosen due to its low superficial area (0.0149 m^2 g^{-1}), as reported elsewhere.[18] When 0.1 M H_2O_2 was added to the test solutions, pH was adjusted to 7.0, prior to catalyst addition. The number of samples was selected to minimize perturbation in the total stock volume. We decided that the sample volume to be withdrawn should be less than 10% of the total volume.

The UV irradiation source was a 10 W Light Emitting Diode (LED, Epistar Co, Taipei, China). The diffraction spectrum of the lamp was obtained with a lab-made spectrophotometer,[36] which showed that the LED had a narrow emission band between 363 nm and 415 nm with a primary peak at 382 nm (Fig. S2c†). Photon flux was measured with a ferrioxalate actinometer[37] and was determined to be 9.9 μeinstein per min. Irradiation intensity was obtained with a digital radiometer (PMA 2100, Solar light, Glenside, PA, USA) with detectors for UV and visible range radiation (PMA 2107 and PMA 2140). The irradiation intensity measured was 4.7 W m^{-2}, distributed 99.6% below 400 nm, which confirms emission occurring at the UV range based on the diffraction spectrum (Fig. S2c†).

2.4. Continuous photocatalytic packed reactor conditions

Reusability and stability were demonstrated through a continuous packed-bed photocatalytic reactor (Fig. S3†). The continuous reactor was a quartz column with dimensions of 1 mm × 10 mm × 100 mm (Fig. S3a†). The column was packed with 2.5 g MicroCuZn (Fig. S3†) and was irradiated with two 10 W LED (UV, Epistar Co, Taipei, China) bulbs. The photon flux was 39.8 μeinstein per min. Experiments were conducted in triplicates and the mean and standard deviation values were reported. The MicroCuZn was reused and ultrasonically washed with acetone, ethanol, and DI water for 10 min, and then dried at 90 °C for 6 h. Experiments were carried out at room temperature (21 ± 1 °C).

2.5. Hydroxyl radical generation

The catalytic and photocatalytic performance were studied with two ˙OH scavengers, *i.e.*, *p*NDA and TA. *p*NDA has been reported previously as an effective ˙OH scavenger;[38,39] however, a recent study suggested that *p*NDA can be susceptible to reductive bleaching.[40] Thus TA was used to confirm and validate effective ˙OH generation.

In aqueous solution and at neutral pH, *p*NDA gives an intense yellow color owing to conjugated double bonds in the molecule with a strong absorption band at 440 nm.[41] When *p*NDA reacts with ˙OH,[39] it becomes colorless at 440 nm;[42] this change is commonly named as *p*NDA bleaching, which was recorded with a Carry 8454 UV-visible spectrophotometer (Agilent Technologies, Santa Clara, CA, USA). The ˙OH generation in the batch reactor, based on *p*NDA bleaching, is described with eqn (1).

$$-\frac{d[p\text{NDA}]}{dt} = k[\text{˙OH}]_{ss}[p\text{NDA}] = k_{obs}[p\text{NDA}] \quad (1)$$

where, [*p*NDA] represents concentration of *p*NDA (M), [˙OH]$_{ss}$ represents steady-state concentration of ˙OH (M), and k_{obs} is the kinetic rate constant.

Photo-hydroxylation reaction of TA produces 2-THA, a fluorescent substance analyzed with an LS-5 fluorescence spectrophotometer (PerkinElmer, Oak Brook, IL, USA) by excitation at λ = 315 nm and fluorescence detection at λ = 425 nm.[43] With a steady-state assumption, ˙OH production in the batch reactor can be calculated with eqn (2).[44]

$$\frac{d[2\text{-THA}]}{dt} = k_r[\text{TA}][\text{˙OH}]_{ss}Y = r_0 \quad (2)$$

where [2-THA] represents 2-THA molar concentration (M), t is time (min), r_0 is a zero-order rate of 2-THA production (M min^{-1}), k_r is the reaction rate constant (4.4 × 10^9 M^{-1} s^{-1}), [˙OH]$_{ss}$ is the steady-state molar concentration (M), and Y is yield as was described earlier.[44] It is to be noted that eqn (1) and (2) though capture the kinetics of ˙OH radical generation, these are utilized to determine reaction rate constants only for the cases when the data collected fit pseudo-first kinetics.

2.6. Analytical methods

E3 and THC concentrations were analyzed with high-performance liquid chromatography (HPLC). HPLC spectra were obtained with a Nexera LC-2040C (Shimadzu Corporation, Kyoto, Japan), equipped with an autosampler, UV-visible detector Shimadzu RF-20A, and a Phenomenex Kinetex column (100 × 4.60 mm; 2.6 μm) kept at 55 °C. The detection of E3 and THC was conducted at 197 nm and 190 nm, respectively. The system used an isocratic mobile phase acetonitrile–water (30 : 70, v/v) at a flow rate of 0.75 mL min^{-1} and an injection volume of 10 μL for E3 detection, and acetonitrile–water (68 : 32, v/v) at a flow rate of 1.0 mL min^{-1} for THC. The detection limit of E3 and THC was 0.1 mg L^{-1} and 0.01 mg L^{-1}, respectively. Dissolved metal concentrations (*i.e.*, for Cu and Zn ions) were quantified with inductively coupled plasma optical emission spectroscopy (ICP-OES) using a Varian 710 ES (Palo Alto, CA) in an argon plasma flame at 7000 K, supported by the ICP Expert II™ software for simultaneous measurement and analysis of all wavelengths of interest. Prior to analysis, samples were diluted by a factor of 10 in 2% (v/v) nitric acid. The detection limit of ICP-OES was 0.01 mg L^{-1} for both Cu and Zn.

3. Results and discussion

3.1. MicroCuZn alloy characterization

The MicroCuZn (Fig. 1a) is a mixture of different sized grains with irregular rounded particles, as shown in representative TEM images (Fig. 1b). MicroCuZn has a density of 2.91 g cm^{-3}.
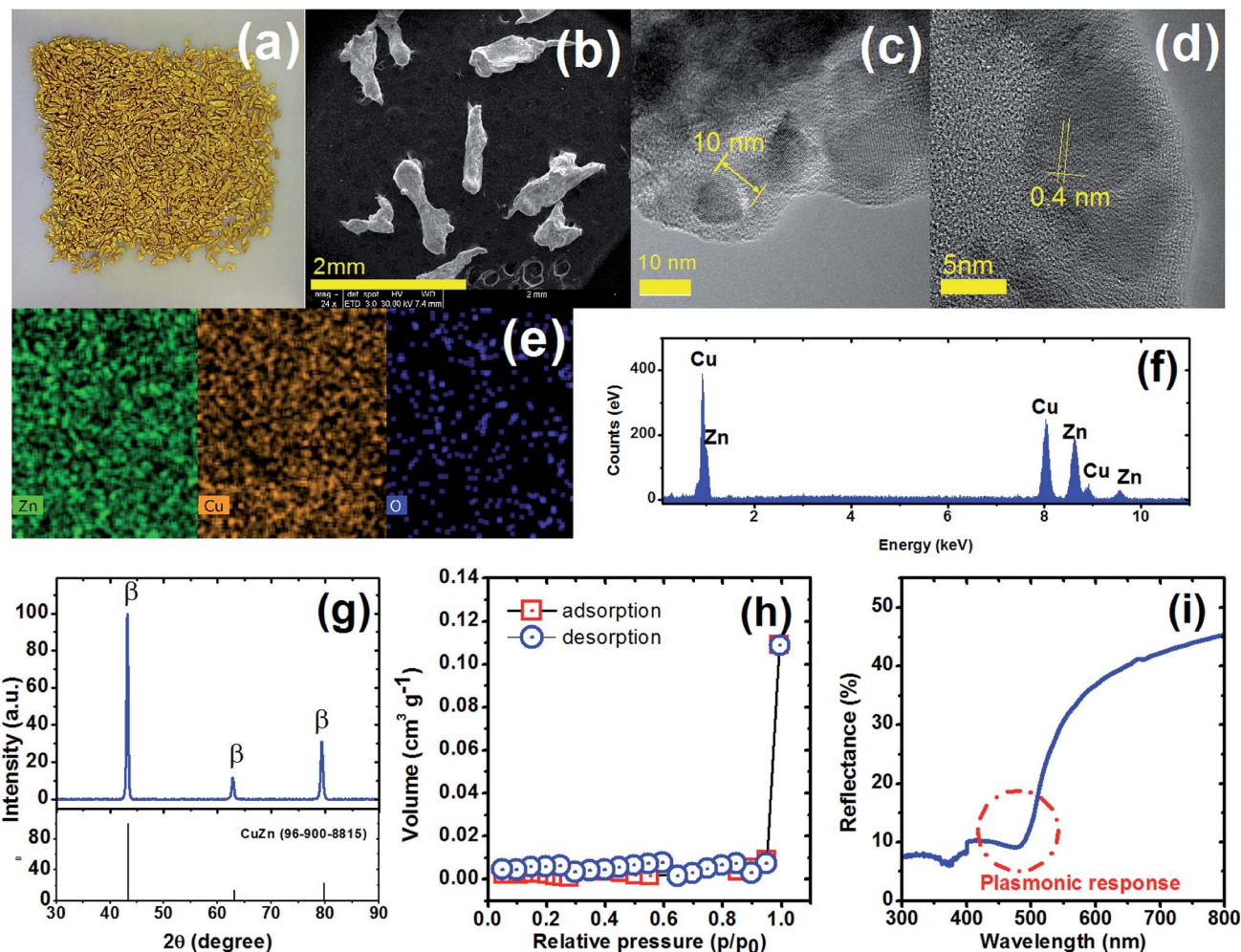
Fig. 1 Optical and morphological characterization of MicroCuZn. (a) Photograph showing MicroCuZn particles; (b) SEM image showing size and shape of MicroCuZn; (c and d) TEM and high-resolution TEM micrographs showing MicroCuZn structure and lattice fringes; (e) SEM/EDS mapping of elemental distribution; (f) elemental composition shown with SEM-EDS spectrum; (g) matching β-phase with experimental data of XRD; (h) nitrogen gas adsorption/desorption hysteresis curves employed in specific BET surface area analysis; and (i) diffuse reflectance spectrum showing plasmonic response in the bulk material near 475 nm.

Maximum and minimum Feret's diameter (Fig. S4†), *i.e.*, the longest and shortest distance between any two points along the particle boundary, are determined to be 0.826 ± 0.144 mm (range 0.44 to 1.11 mm) and 0.496 ± 0.09 mm (range 0.31 to 0.69 mm), respectively. Average projected area (Fig. S4d†) is estimated to be 0.261 ± 0.068 mm^2 (range 0.11 to 0.41 mm^2) with circularity of 0.482 ± 0.126 (range 0.21 to 0.77); which indicate elongated materials (Fig. S4†).

High-resolution TEM micrographs show 10 nm wide crystals (Fig. 1c), having defined lattice fringes with 0.4 nm spacing (Fig. 1d). The elemental distribution appears to be homogeneous (Fig. 1e) with 47.2 wt% copper, 44.4 wt% zinc. Other detected elements form the EDS analysis are shown in Table S1.† According to the Cu and Zn content, the MicroCuZn composition corresponds to the α + β phase as observed in the phase diagram; the analysis is based on Kaprara *et al.*[12] method (Fig. S5†). XRD analysis (Fig. 1g) further confirms the dominance of the β-phase with defined peaks at 43.36° and 79.47°,

when compared with the Crystallography Open Database (card 9008814).[31] Kaprara *et al.*[12] suggested (1 0 0) crystal planes in MicroCuZn, which are a result of the crystallization process.

The specific BET surface area (Fig. 1h) is determined to be 0.003 m^2 g^{-1}. Based on the International Union of Pure and Applied Chemistry (IUPAC) classification,[45] the isotherm in Fig. 1h indicates a reversible type II behavior, obtained with a non-porous or macroporous adsorbent. The surface homogeneity can be confirmed by comparing the specific surface area and the specific external surface area (eqn (3)).

$$\gamma = \frac{S_e}{m_p} \approx \frac{2a}{m} \tag{3}$$

where, γ is specific external surface area (m^2 g^{-1}), S_e is particle surface area (m^2), m_p is particle weight (g^{-1}), a is average projected area (m^2), m is average particle weight (g^{-1}). Considering that the average particle has Ferret diameter (a) and that its average weight is 0.009 ± 0.003 mg, γ is determined to be 0.029

$\pm$ 0.0015 m^2 g^{-1}, which is in the same order of magnitude as the one obtained from the specific surface area analysis; these results confirm that the catalyst particles are likely non-porous, thus the catalytic or adsorption processes will likely take place on the surface of the catalyst.

The diffuse reflectance spectrum (Fig. 1i) shows a sharp decrease and then an increase near 475 nm (2.6 eV), which suggest a plasmonic response in MicroCuZn. The plasmonic response in the bulk β-phase is suggesting that the optical property is due to the inter-band transition from Fermi level (E_f) to the vacant conduction sp states.[46,47]

3.2. Removal of E3 and THC from water

Fig. 2a shows that E3 removal in dark is negligible, while MicroCuZn can remove only <4% of E3 after 48 h. The low E3 (with log K_{ow} = 2.45) removal is likely due to adsorptive partitioning, which agrees well with low sorption propensity showed on activated carbon.[48] E3 shows a slow decrease in the presence of H$_2$O$_2$, likely due to the generation of $^{\bullet}$OH (eqn (4)) in the presence of this oxidant.[49]

$$H_2O_2 \rightarrow OH^- + {}^{\bullet}OH \rightarrow 1/2O_2 + 2H_2O \tag{4}$$
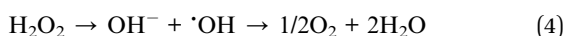
$^{\bullet}$OH is generated in the presence of H$_2$O$_2$ at pH 7.0 and above. It is to be noted that all experiments for contaminant removal have been conducted in pH 7.0, while the terephthalic acid (TA) measurements were conducted at pH 9.0 (to ensure solubility of TA). TA is a substance that reacts with $^{\bullet}$OH radical and the responses measured for 2-THA production indicate $^{\bullet}$OH radical production. Data presented in Fig. S6† shows that, MicroCuZn under UV irradiation produces $^{\bullet}$OH radicals. However, uncatalyzed decomposition of H$_2$O$_2$ can take place because of temperature, pH, surface effects, impurities, and photo-radiation.[50]

E3 decay increases when MicroCuZn and H$_2$O$_2$ react in concert and reaches 84.3% removal in 48 h. Such decay is likely caused by corrosion of the catalyst (eqn (5))[20] that produces $^{\bullet}$OH radicals via catalytic H$_2$O$_2$ disproportionation near the catalyst–water interface and by Fenton-like reaction of Cu in the bulk water (eqn (6) and (7)).[35,51] Zhou et al. suggested that Cu$^+$ could be released following the reaction pathway shown in eqn (6).[51]
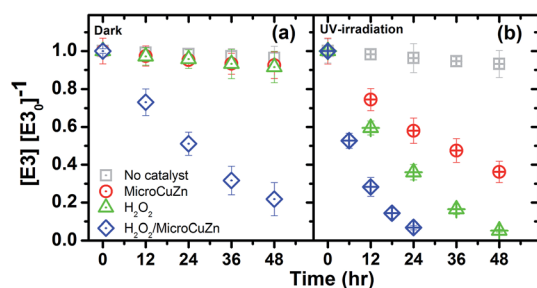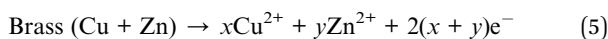
$$\text{Brass (Cu + Zn)} \rightarrow x\text{Cu}^{2+} + y\text{Zn}^{2+} + 2(x+y)\text{e}^- \tag{5}$$

$$\text{Cu}^0_{(s)} + 1/2H_2O_2 \rightarrow \text{Cu}^+ + OH^- \tag{6}$$

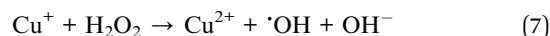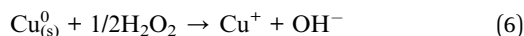$$\text{Cu}^+ + H_2O_2 \rightarrow \text{Cu}^{2+} + {}^{\bullet}OH + OH^- \tag{7}$$

Fig. 2b shows E3 removal under UV irradiation. E3 degradation by photolysis alone (i.e., in the absence of any catalyst or oxidant) is 3.1% after 48 h; this result is significantly lower than the previously reported photo-removal of E3 that used a back-light fluorescent lamp and a germicidal lamp.[52] The decreased photo-removal can be attributed to the intensity and the emission peak of the lamp, which did not overlap with the molar absorption of E3 in this study (Fig. S7†).

E3 considerably decreases in the UV/MicroCuZn system, with 62.7% removal after 48 h, which is significantly higher than the extent of removal observed with the catalyst in the dark (Fig. 2a). The rate of decay followed pseudo-first-order kinetics with a rate constant of 0.335 × 10^{-3} min^{-1} (r^2 = 0.996). The removal was likely because of the direct $^{\bullet}$OH attack of E3 and h$^+$ oxidation. This assumption is based on that photocorrosion of brass that can produce ROS, as shown by others.[23] Dissolved O$_2$ and H$_2$O$_2$ causes brass corrosion when irradiated with UV. Cu/Zn ratio in brass is a critical factor in determining the susceptibility of dezincification; e.g., brass with zinc content of ~15% is generally considered resistant to dezincification.[53] Lin and Frankel studied atmospheric corrosion of copper and found that UV promotes Cu$_2$O formation.[54] Zhang et al. verified the presence of hydrozincite, simonkolleite, and CuO, Cu$_2$O, ZnO in the corrosion products of brass with 40% Cu content.[55] Sun et al. demonstrated that UV irradiation promoted atmospheric corrosion of brass alloy and detected formation of Cu(OH)$_2$, CuO, and Cu$_2$O in dark, and CuO, Cu$_2$O, ZnO, Zn$_5$(OH)$_8$C$_{12}$·H$_2$O, Zn$_5$(CO$_3$)$_2$(OH)$_6$ when UV-irradiated.[22] Ibrahim et al. found copper corrosion in the presence and absence of a low gamma irradiation and cited formation of Cu$_2$O.[23] Zhdan and Castle demonstrated CuO growth on the surface of brass.[56] Even though, E3 may be prone to degradation and thereby produce less estrogenic compounds[57] and to mineralization because of $^{\bullet}$OH attacks,[58] further studies are necessary to unravel the mechanisms underlying such photo-removal.

The E3 concentration substantially decreases in UV/H$_2$O$_2$ system; i.e., by 94.7% after 48 h, which is significantly greater than H$_2$O$_2$ oxidation in the dark. Such a decrease may be attributed to the UV-mediated (i.e., emitting between 363 nm and 415 nm) photolysis of H$_2$O$_2$, as shown in eqn (8).[59] It has been reported that H$_2$O$_2$ photolysis is effective at wavelength lower than 380 nm.[60] The E3 degradation by H$_2$O$_2$ with low- and medium-pressure mercury lamp irradiation has been well-documented.[61]

$$H_2O_2 + hv \rightarrow 2^{\bullet}OH \tag{8}$$

The systematic increase in the rate of E3 degradation (Fig. 2) is an illustration of the possible synergy between the irradiating UV energy, oxidizing agent H$_2$O$_2$ and the catalyst MicroCuZn. The UV/H$_2$O$_2$/MicroCuZn system accomplishes the fastest E3 degradation, following pseudo-first-order kinetics with a decay rate constant of 1.853 × 10^{-3} min^{-1} (r^2 = 0.999); this value is three times greater than the H$_2$O$_2$/MicroCuZn system in the

Fig. 2 E3 degradation (10 μM, pH 7) with MicroCuZn (10 g L^{-1}) at 20 °C and with H$_2$O$_2$ (0.1 M); (a) in dark and (b) under UV-irradiation (9.9 μeinstein per min).

dark. The extent of removal in this case is the greatest among all conditions studied. The absence of the catalyst or that of H_2O_2 has shown to decrease the E3 degradation rate.

The electrical energy per order (E_{EO}) index is used to assess efficiency in terms of electrical energy consumption for degrading contaminants.[62] E_{EO} index for $UV/H_2O_2/MicroCuZn$ is obtained as 1.03×10^3 kW h m^{-3}; which is the lowest of all the values, indicating that this condition is the most energy efficient. The E_{EO} value estimated here is consistent with the reported advanced oxidation energy efficiency for $UV/H_2O_2/$ MicroCuZn, presented in Miklos *et al.*[63] This material thus can become a practical, effective, and energy-efficient option for oxidative E3 removal from water.

Fig. 3 shows that THC concentration decreases over time in both dark and UV irradiated conditions. In dark, the glass reactor and MicroCuZn exhibit significant adsorption for THC, with 81.2% and 91% of removal over 300 min, respectively. It seems THC's hydrophobicity (log K_{ow} > 5) and electrostatic attraction towards MicroCuZn and silicates (within the glass) are likely responsible for such adsorption.[27,64,65] The THC results indicate that the removal is caused by a combination of adsorption and possible photoreaction. After adsorption, THC may be oxidized *via* ˙OH radicals. The complete mineralization of THC towards CO_2 and H_2O may take place by photocatalytic and heterogeneous photo-Fenton treatment.[65,66] It is to be noted that contribution of photoreaction alone in the removal of this hydrophobic compound, cannot be tweezed out.

THC removal in the dark/no catalyst and UV/no catalyst conditions are determined to be 81.2% and 74%, respectively. It can thus be concluded that THC photolysis is not the dominant removal process upon 300 min of UV irradiation. Not only that the intensity and emission peaks of the lamps do not overlap with THC molar absorption in the UV-visible region (Fig. S7†), as was also the case for E3, extent of THC adsorption on the glass container might have been influenced during UV irradiation. That is, localized heating of the glass surfaces or radicals

generated (in the solution) during the irradiation process could have contributed to partial desorption of THC from glass, thus reduced the overall removal when compared to the catalyst-free case in the dark. Special reactors (*e.g.*, silanized glass) to suppress THC adsorption onto glass can be utilized for untangling photo-catalytic removal from that *via* adsorption.

3.3. Hydroxyl radical production

We hypothesized in Section 3.2 that E3 removal is primary caused by photoreaction with ROS, in particular from ˙OH. *p*NDA is a ˙OH probe, that is useful for measuring the photo-catalytic performance in water treatment with the following advantages: (i) it has selective 1 : 1 reactivity with ˙OH,[67–70] (ii) it has a high reaction rate with ˙OH, which is in the order of 10^{10} M^{-1} s^{-1} (ref. 70 and 71) and (iii) it does not react with singlet oxygen ($^1O_2$), superoxide anions ($O_2^{\cdot-}$) or other peroxy compounds.[41] Generation of ˙OH is measured with *p*NDA bleaching under identical experimental conditions.

In general, *p*NDA bleaching (see Fig. 4) in the dark and under UV irradiation follows similar trend as observed in Fig. 2. In the dark (Fig. 4a), *p*NDA blank stays unchanged, while it slightly decreases (about 10%) owing to adsorption onto MicroCuZn. Similar observation has been reported earlier for aniline adsorption onto brass.[72] A decrease of 15% is detected due to ˙OH generation in the presence of H_2O_2 (eqn (4)). *p*NDA bleaching was also reported earlier at an elevated temperature (50 °C).[73]

The concentration of *p*NDA decreases rapidly due to ˙OH production in the presence of H_2O_2, which then catalyzes MicroCuZn. ˙OH production under this condition followed a catalytic reaction on the MicroCuZn surface in the dark and Fenton-like reaction at neutral pH (eqn (6) and (7)). Excess H_2O_2 in the solution may accelerate MicroCuZn corrosion and thereby cause leaching of Cu and Zn ions into the bulk solution.[74] Pham *et al.*[75] confirmed that Fenton-like reaction can be initiated by Cu ions at neutral pH and Hobbs and Abbot[73] reported *p*NDA bleaching by ionic Cu at comparable magnitude as measured in this study. H_2O_2 can reduce Cu^{2+}, generating $O_2^{\cdot-}$ and Cu^+, which then can catalyze H_2O_2 to produce ˙OH and Cu^{2+} (eqn (6) and (7)). Conversely, it has been reported that Zn^{2+} does
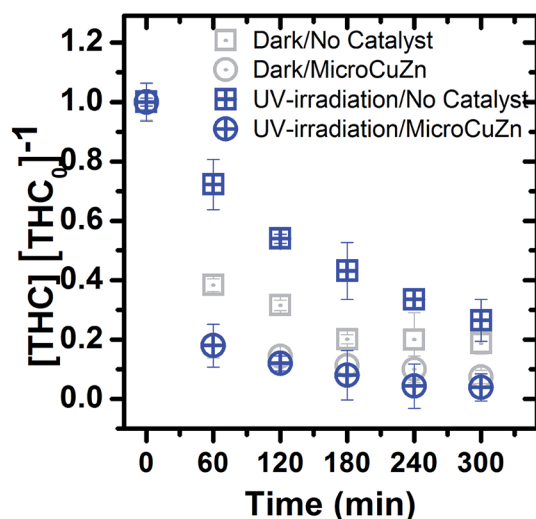

Fig. 3 THC concentration history (1 μM initial concentration at pH 7) to elucidate MicroCuZn (10 g L^{-1}) catalysis effects. Experiment were conducted at 20 °C and UV-irradiation was 9.9 μeinstein per min.

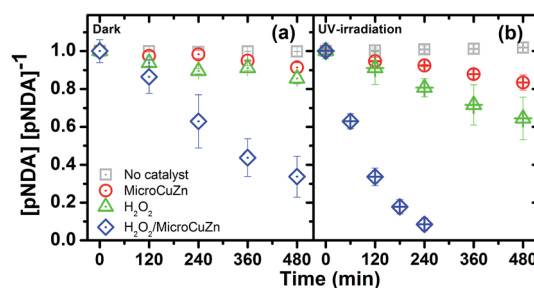Fig. 4 *p*NDA bleaching (10 μM, pH 7) with MicroCuZn (10 g L^{-1}) at 20 °C and with needed H_2O_2 (0.1 M); (a) in dark and (b) under UV irradiation (9.9 μeinstein per min). Note that pH values have been measured before and after the experiments and are reported in Table S2.†

not significantly influence the formation of ˙OH in a Fenton-like reaction.[76]

H_2O_2 can be decomposed[50] and catalyzed[75,77,78] by Cu^{2+} to produce ˙OH, causing Cu^+ and Cu^{2+} dissolution. However, at pH 7 (*i.e.*, the condition used in the contaminant degradation experiments), Cu^+ and Cu^{2+} ions form stable CuOH and $Cu(OH)_2$ species, respectively (eqn (9)–(11)), which can subsequently redeposit and form Cu_2O.[35]

$$Cu^+ + OH^- \rightarrow CuOH \qquad (9)$$

$$Cu^{2+} + OH^- \rightarrow Cu(OH)_2 \qquad (10)$$

$$2CuOH \rightarrow Cu_2O + H_2O \qquad (11)$$
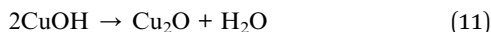
*p*NDA is reduced at a moderate rate in the UV/MicroCuZn system because of ˙OH attacks. A recent study has questioned the selectivity of *p*NDA to ˙OH, suggesting that *p*NDA bleaching could be due to a reduction reaction.[40] To probe this question, TA is used to assess MicroCuZn photocatalytic activity (in UV/MicroCuZn system). 2-THA generation shown in Fig. S7† confirms that UV/MicroCuZn can produce ˙OH. The evidence of ˙OH generation is detected from not only *p*NDA bleaching but also from 2-THA fluorescence in MicroCuZn/UV system, which supports the assumption that MicroCuZn photocatalytic activity is caused by the ˙OH attack.

It is well known that when the MicroCuZn alloy is used in a catalytic process, oxidation of Cu and Zn takes place, which leads to formation of CuO, Cu_2O, ZnO.[23,79] Furthermore, when ZnO and Cu_xO combine, a (p–n) heterojunction is formed,[80,81] which is effective in enhanced utilization of photoenergy and modulation of e^-/h^+ recombination. Though it is challenging to pin point electron excitation and transfer within a complex alloy (and subsequent oxidized form of the alloy) through measurements, reasonable analysis can be made and conclusions can be drawn from the energetic band positioning of the oxidized forms of Cu and Zn.

Typically, upon photo-irradiation, promotion of electrons to the conduction band (CB), leaves holes behind at the valence band (VB). The excited or hot-electrons (e^-) are known to transfer to the surrounding dissolved oxygen molecules and produce ˙O_2^-, while holes (h^+) are known to transfer to $^-$OH and produce ˙OH. O_2^- is also known to form ˙OH through a cascading reaction sequence[82] while recombination of e^-/h^+ pair can compromise the radical production process. In the complex mixture of Cu_xO/ZnO, the relative positioning of VB for Cu_2O makes electron excitation to the CB of this oxide phase, likely (Fig. 5a). The UV irradiation at 363 nm to 415 nm wavelength provides necessary photo-energy for hot e^- production, not only from the Cu_2O, but also from the other two oxide phases (*i.e.*, CuO and ZnO as shown in Fig. 5b). Hot e^- generated within the Cu_2O phase can migrate to the CB of either ZnO and CuO, while the photogenerated h^+ from these phases can migrate toward the VB of the Cu_2O phase.[81] Such e^- and h^+ transfer within the complex oxide phases of the alloy likely modulates (*i.e.*, delays or prevents) recombination of the photogenerated e^-/h^+ pair.[81]
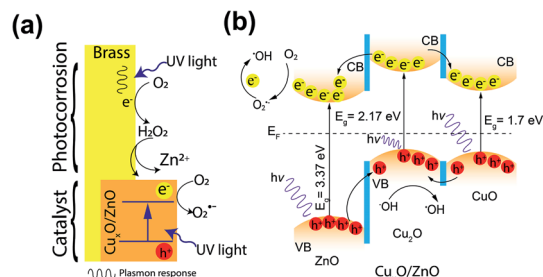

Fig. 5 Photocatalytic mechanism on MicroCuZn surface: (a) photocorrosion initiation and formation of patches; and (b) electron–hole transfer mechanism with hydroxyl radical generation where CB is conduction band, VB is valence band, and E_f is Fermi level.[81]

In order to corroborate the formation of a complex oxide film (ZnO/Cu_xO), XPS analyses were conducted. Fig. 6 shows the overall and deconvoluted XPS spectra obtained for samples in the dark and those exposed to UV irradiation for 12 h. The overall spectrum (Fig. 6a) shows O, C, Zn, and Cu characteristic peaks, where the high intensity Zn $2p_{3/2}$ peaks have likely occurred due to the high zinc content within MicroCuZn. Specific XPS spectra of Cu $2p_{3/2}$ region (Fig. 6b and c) show a significant decrease in the $Cu(OH)_2$ peak and an increase in the Cu_2O peak. Ibrahim *et al.*[23] suggested that Cu corrosion can lead to CuO–Cu_2O formation. Zn $2p_{3/2}$ region deconvolution (Fig. 6d and e) shows that the UV irradiated case has an increase in metallic zinc content (Zn(0)). Such increase may be due to the Zn atoms rearrangement, as suggested by Zhou.[83]

The complex oxide film formation is guided by the reactions under non-irradiated and irradiated conditions. In non-irradiated conditions, selective leaching of Zn occurs to form Cu-rich areas.[84] Such dezincification of the surfaces has been intensively investigated elsewhere,[56,85] however, a consensus on formation mechanism has not been reached.[83] It can be hypothesized that preferential dissolution of Zn from the Cu–Zn lattice will likely take place due to zinc's equilibrium potential being more negative, when compared to Cu.[83] It is also important to note that upon dezincification formation of zinc hydroxide or oxides may take place.[86] Whittle *et al.* suggested that ZnO can be formed due to reaction with Cu_2O that can generate patchy mixed oxide phases of Cu_xO/ZnO on the MicroCuZn surfaces.[87] Furthermore, Cu-rich areas can be oxidized to Cu_2O[88] and subsequently to CuO,[23] eventually leading to growth of Cu_xO patches. Moreover, H_2O_2 can be decomposed[50] and catalyzed[75,77,78] by Cu^{2+} to produce ˙OH, causing Cu^+ and Cu^{2+} dissolution and redeposition. However at pH 7, Cu^+ and Cu^{2+} forms stable oxide forms CuOH and $Cu(OH)_2$, respectively, which can also redeposit and form Cu_2O.[35] UV irradiation may increase the dezincification of brass[89] and consequently may increase the Cu-rich areas.

This also indicates that the photocatalytic activity of the catalyst may have been caused by the increase of the number of semiconductor-like areas or patches on the surface. Recently, it has been reported Zn/Cu_xO is an effective photocatalyst for water treatment[90,91] or for water splitting.[92]
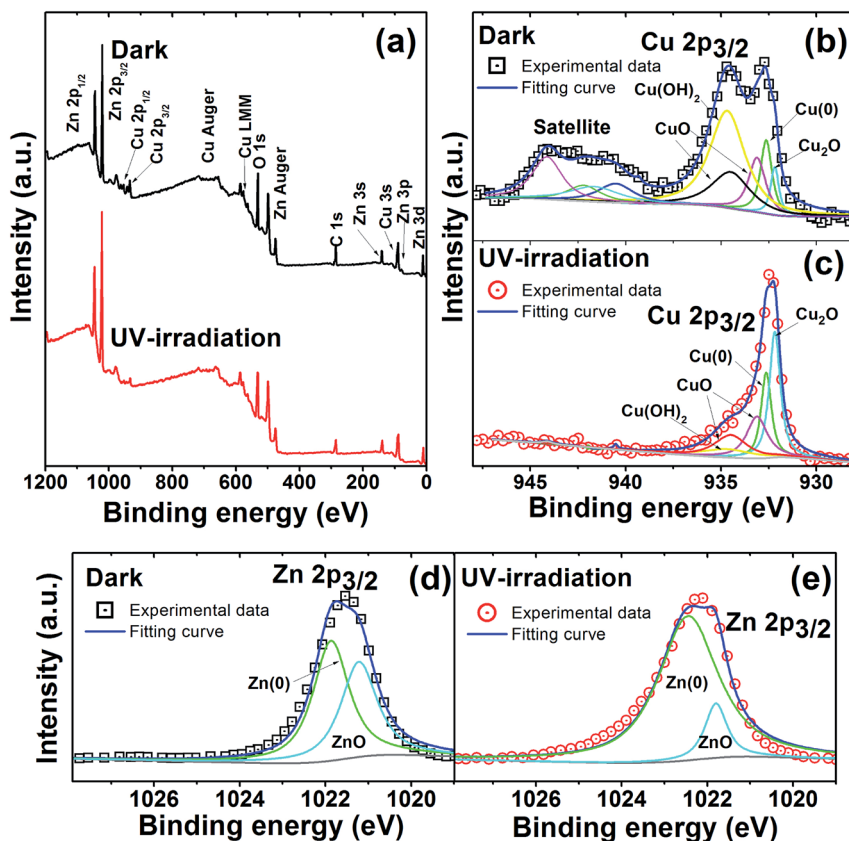
Fig. 6 (a) Overall XPS spectrum with identified characteristic peaks for MicroCuZn in dark and when UV irradiated over 12 h in deionized water. Deconvoluted XPS spectra for Cu 2p$_{3/2}$ region in (b) dark and when (c) UV-irradiated. Deconvoluted XPS spectra for Zn 2p$_{3/2}$ region in (d) dark and when (e) UV-irradiated.
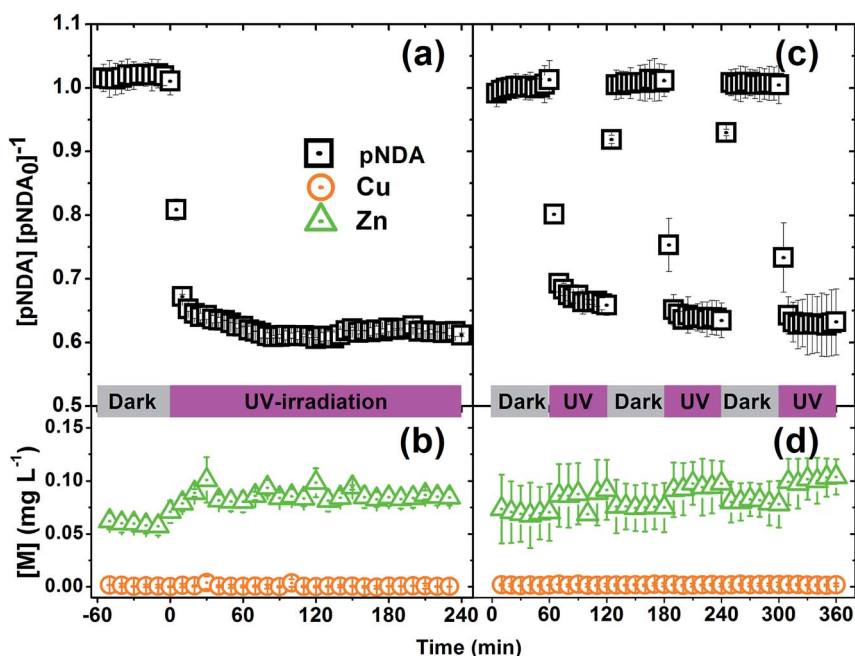

Fig. 7 Photocatalytic activity of MicroCuZn in a continuous packed photocatalytic reactor (1 mL min^{-1}) for the pNDA bleaching (10 μM, pH 7). Stability shown via (a) photobleaching history and (b) low propensity of metal leaching. Performance under cyclic in dark and illuminated conditions show with (c) cyclic recovery of photobleaching ability and (d) low propensity of metal leaching.

3.4. Reusability of MicroCuZn photocatalytic activity

Reusability and stability of MicroCuZn is shown in Fig. 7, where the left panels show *p*NDA signal strength and dissolved Cu and Zn concentration under a prolonged irradiation condition (4 h flow through operation at 1 mL min^{-1}); while the panels on the right show the same for an alternating irradiating and dark condition cycling. Fig. 7a shows that *p*NDA bleaching remains unchanged during the dark phase, followed by a strong bleaching phase when the catalyst is activated under UV irradiation. The alternating dark-illuminated cyclic exposure of the catalyst show effectiveness of *p*NDA bleaching at the same extent, even after three cycles of use (Fig. 7c). Fig. 7b and d demonstrate that the MicroCuZn catalysts are stable and do not dissolve ionic Cu (<0.01 mg L^{-1}) or Zn (<0.1 mg L^{-1}) significantly.

4.   Conclusions

Characterization of MicroCuZn confirmed that commercially available KDF® 55 was a β-brass with homogenous elemental distribution and plasmonic response near 475 nm. H$_2$O$_2$ increased its catalytic activity. The material was shown to degrade two structurally relevant model ECs with phenolic moieties and high octanol–water partitioning coefficients (*i.e.*, both highly hydrophobic). The photodegradation and removal from water were systematically evaluated to unravel the underlying mechanisms. Photocatalytic mechanism of Micro-CuZn was likely initiated in CuZn alloy crystalline arrays by the plasmonic response, which introduced hot electrons that can be transferred to the neighboring dissolved oxygen molecules to produce ˙O$_2$$^{-}$. These radicals caused brass corrosion to initiate a cascading reaction sequence for ˙OH generation. When MicroCuZn is stimulated with UV radiation, a semiconductor oxide film grew on the MicroCuZn surfaces. We suggest that a mixture of ZnO, CuO, and Cu$_2$O may be responsible for MicroCuZn photocatalytic activity for E3 removal. On the other hand, adsorption effect was observed to be a critical process for THC removal from water, while photocatalysis mildly enhance the removal efficacy.

Micron-scale brass can be effectively applied for oxidative removal of ECs. These micron-scale alloys can be considered as promising photo-oxidative alternatives considering their low-cost, earth-abundancy, stability during reaction, and potential reusability. In addition, these catalysts are considered non-toxic because of their low-leaching potential. Further research is necessary to evaluate the efficacy of these materials in a more complex aquatic background (*e.g.*, in the presence of natural organic matter, turbidity, ionic strength, *etc.*) as well as to test their effectiveness in environmentally pertinent levels of ECs (*i.e.*, at ng L^{-1}) in continuous reactors. Such studies will facilitate transferability of these materials from laboratory to engineering practice. Mechanistic understanding of the pollutant degradation pathways that are elucidated here will enable strategic micro-brass synthesis for water treatment purposes and facilitate future engineering solutions (*e.g.*, reactor design and material recovery) for municipal level or point-of-use water

treatment systems and ensure safe and sustainable deployment of this millennia-old alloy as an effective catalyst.

Conflicts of interest

There are no conflicts to declare.

Acknowledgements

References

1 B. Petrie, R. Barden and B. Kasprzyk-Hordern, A review on emerging contaminants in wastewaters and the environment: current knowledge, understudied areas and recommendations for future monitoring, *Water Res.*, 2015, **72**, 3–27.

2 O. M. Rodriguez-Narvaez, J. M. Peralta-Hernandez, A. Goonetilleke and E. R. Bandala, Treatment technologies for emerging contaminants in water: a review, *Chem. Eng. J.*, 2017, **323**, 361–380.

3 G. Crini and E. Lichtfouse, Advantages and disadvantages of techniques used for wastewater treatment, *Environ. Chem. Lett.*, 2019, **17**, 145–155.

4 G. Grass, C. Rensing and M. Solioz, Metallic copper as an antimicrobial surface, *Appl. Environ. Microbiol.*, 2011, **77**, 1541–1547.

5 G. Bottari, A. J. Kumalaputri, K. K. Krawczyk, B. L. Feringa, H. J. Heeres and K. Barta, Copper-Zinc Alloy Nanopowder: A Robust Precious-Metal-Free Catalyst for the Conversion of 5-Hydroxymethylfurfural, *ChemSusChem*, 2015, **8**, 1323–1327.

6 Y. Feng, Z. Li, H. Liu, C. Dong, J. Wang, S. A. Kulinich and X. Du, Laser-Prepared CuZn Alloy Catalyst for Selective Electrochemical Reduction of CO$_2$ to Ethylene, *Langmuir*, 2018, **34**, 13544–13549.

7 A. Chafidz, Megawati, C. R. Widyastuti, V. Augustia, K. Nisa and Ratnaningrum, Application of copper-zinc metal as a catalytic converter in the motorcycle muffler to reduce the exhaust emissions, *IOP Conf. Ser. Earth Environ. Sci.*, 2018, **167**, 1–8.

8 F. Fu, Z. Cheng and J. Lu, Synthesis and use of bimetals and bimetal oxides in contaminants removal from water: a review, *RSC Adv.*, 2015, **5**, 85395–85409.

9 A. Zaleska-Medynska, M. Marchelek, M. Diak and E. Grabowska, Noble metal-based bimetallic nanoparticles: the effect of the structure on the optical, catalytic and photocatalytic properties, *Adv. Colloid Interface Sci.*, 2016, **229**, 80–107.

10 J.-H. Richard and H. Biester, Mercury removal from contaminated groundwater: performance and limitations of amalgamation through brass shavings, *Water Res.*, 2016, **99**, 272–280.

11 H. S. Majdi, M. S. Jaafar and A. M. Abed, Using KDF material to improve the performance of multi-layers filters in the reduction of chemical and biological pollutants in surface water treatment, *S. Afr. J. Chem. Eng.*, 2019, **28**, 39–45.

12 E. Kaprara, P. Seridou, V. Tsiamili, M. Mitrakas, G. Vourlias, I. Tsiaoussis, G. Kaimakamis, E. Pavlidou, N. Andritsos and K. Simeonidis, Cu-Zn powders as potential Cr(VI) adsorbents for drinking water, *J. Hazard. Mater.*, 2013, **262**, 606–613.

13 A. Sites and L. Oberholtzer, *Mercury point-of-entry treatment study*, unpublished report, NJ Department of Environmental Protection and Energy, Trenton, NJ, 1992, p. 43.

14 D. P. Fourness, Evaluation of Decentralized Alternatives for Separate Treatment and Supply of Indoor Water: Fort Collins Case Study, MSc thesis, Color. State Univ., 2015, 154.

15 N. A. Hanks, Silver Nanoparticle and Silver Ion Water Contamination: Assessment of Phytoremediation and Point-of-use Filtration Media, PhD thesis, University of Cincinnati, 2015, p. 128.

16 A. Carrière, M. Brouillon, S. Sauvé, M. F. Bouchard and B. Barbeau, Performance of point-of-use devices to remove manganese from drinking water, *J. Environ. Sci. Health, Part A: Toxic/Hazard. Subst. Environ. Eng.*, 2011, **46**, 601–607.

17 K. Jing, X. Guo, Y. Jiang, Q. Wu, S. Wang, X. Shi, N. Zhou and Z. Zhu, Removal of Antimony(III) from Aqueous Solutions Using Copper-Zinc Alloy Filter Media, *Open Journal of Water Pollution and Treatment*, 2014, 1–10.

18 A. Catennaci, Heavy metal removal from water: characterization and applicability of unconventional media, PhD thesis, Politecnico di Milano, 2014, p. 129.

19 Q. Wang, Y. Zhang, H. Wang and L. Ma, A pathway of free radical generation via copper corrosion and its application to oxygen and ozone activation for the oxidative destruction of organic pollutants, *Res. Chem. Intermed.*, 2018, **44**, 7391–7410.

20 F. M. Al Kharafi, I. M. Ghayad and R. M. Abdullah, Effect of hydrogen peroxide on the dezincification of brass in acidified sodium sulfate solution under free corrosion conditions, *J. Mater. Environ. Sci.*, 2010, **1**, 58–69.

21 T. D. Burleigh, C. Ruhe and J. Forsyth, Photo-Corrosion of Different Metals during Long-Term Exposure to Ultraviolet Light, *Corrosion*, 2003, **59**, 6.

22 X. Sun, Initial NaCl-induced atmospheric corrosion of a dual-phase Cu60-40Zn alloy - Effect of UV illumination, *Int. J. Electrochem. Sci.*, 2018, **13**, 8150–8169.

23 B. Ibrahim, D. Zagidulin, M. Behazin, S. Ramamurthy, J. C. Wren and D. W. Shoesmith, The corrosion of copper in irradiated and unirradiated humid air, *Corros. Sci.*, 2018, **141**, 53–62.

24 Å. Björkbacka, C. M. Johnson, C. Leygraf and M. Jonsson, Radiation Induced Corrosion of Copper in Humid Air and Argon Atmospheres, *J. Electrochem. Soc.*, 2017, **164**, C201–C206.

25 S. Deng, H. Lu and D. Y. Li, Influence of UV light irradiation on the corrosion behavior of electrodeposited Ni and Cu nanocrystalline foils, *Sci. Rep.*, 2020, **10**, 3049.

26 O. G. Apul, L. S. Rowles, A. Khalid, T. Karanfil, S. D. Richardson and N. B. Saleh, Transformation potential of cannabinoids during their passage through engineered water treatment systems: a perspective, *Environ. Int.*, 2020, **137**, 105586.

27 A. Khalid, L. S. Rowles, M. Ateia, M. Xiao, I. Ramirez-Sanchez, D. Bello, T. Karanfil, N. B. Saleh and O. G. Apul, Mesoporous activated carbon shows superior adsorption affinity for 11-nor-9-carboxy-Δ9-tetrahydrocannabinol in water, *npj Clean Water*, 2020, **3**, 2.

28 N. B. Saleh, O. Apul and T. Karanfil, The Genesis of a Critical Environmental Concern: Cannabinoids in Our Water Systems, *Environ. Sci. Technol.*, 2019, **53**, 1746–1747.

29 Z. Liu, G. Lu, H. Yin and Z. Dang, Do we underestimate the concentration of estriol in raw municipal wastewater?, *Environ. Sci. Pollut. Res.*, 2015, **22**, 4753–4758.

30 M. Adeel, X. Song, Y. Wang, D. Francis and Y. Yang, Environmental impact of estrogens on human, animal and plant life: a critical review, *Environ. Int.*, 2017, **99**, 107–119.

31 A. Altomare, N. Corriero, C. Cuocci, A. Falcicchio, A. Moliterni and R. Rizzi, QUALX2.0: a qualitative phase analysis software using the freely available database POW_COD, *J. Appl. Crystallogr.*, 2015, **48**, 598–603.

32 M. C. Biesinger, Advanced analysis of copper X-ray photoelectron spectra, *Surf. Interface Anal.*, 2017, **49**, 1325–1334.

33 M. C. Biesinger, L. W. M. Lau, A. R. Gerson and R. S. C. Smart, Resolving surface chemical states in XPS analysis of first row transition metals, oxides and hydroxides: Sc, Ti, V, Cu and Zn, *Appl. Surf. Sci.*, 2010, **257**, 887–898.

34 K. Ishibashi, A. Fujishima, T. Watanabe and K. Hashimoto, Detection of active oxidative species in TiO₂ photocatalysis using the fluorescence technique, *Electrochem. Commun.*, 2000, **2**, 207–210.

35 P. V. F. de Sousa, A. F. de Oliveira, A. A. da Silva and R. P. Lopes, Environmental remediation processes by zero valence copper: reaction mechanisms, *Environ. Sci. Pollut. Res.*, 2019, **26**, 14883–14903.

36 R. D. Lorenz, A simple webcam spectrograph, *Am. J. Phys.*, 2014, **82**, 169–173.

37 S. L. Murov, I. Carmichael and G. L. Hug, *Handbook of Photochemistry*, CRC Press, New York, NY, 2nd edn, 1993.

38 N. Nordin, L.-N. Ho, S.-A. Ong, A. H. Ibrahim, A. L. Abdul Rani, S.-L. Lee and Y.-P. Ong, Hydroxyl radical formation in the hybrid system of photocatalytic fuel cell and peroxi-coagulation process affected by iron plate and UV light, *Chemosphere*, 2020, **244**, 125459.

39 I. Kraljic and C. N. Trumbore, p-Nitrosodimethylaniline as an OH radical scavenger in radiation chemistry, *J. Am. Chem. Soc.*, 1965, **87**, 2547–2550.

40 S. Mortazavian, E. R. Bandala, J.-H. Bae, D. Chun and J. Moon, Assessment of p-nitroso dimethylaniline (pNDA) suitability as a hydroxyl radical probe: investigating bleaching mechanism using immobilized zero-valent iron nanoparticles, *Chem. Eng. J.*, 2020, **385**, 123748.

41 M. E. Simonsen, J. Muff, L. R. Bennedsen, K. P. Kowalski and E. G. Søgaard, Photocatalytic bleaching of p-nitrosodimethylaniline and a comparison to the performance of other AOP technologies, *J. Photochem. Photobiol., A*, 2010, **216**, 244–249.

42 J. Muff, L. R. Bennedsen and E. G. Søgaard, Study of electrochemical bleaching of p-nitrosodimethylaniline and its role as hydroxyl radical probe compound, *J. Appl. Electrochem.*, 2011, **41**, 599–607.

43 L. T. T. Tuyen, D. A. Quang, T. T. Tam Toan, T. Q. Tung, T. T. Hoa, T. X. Mau and D. Q. Khieu, Synthesis of CeO_2/TiO_2 nanotubes and heterogeneous photocatalytic degradation of methylene blue, *J. Environ. Chem. Eng.*, 2018, **6**, 5999–6011.

44 S. E. Page, W. A. Arnold and K. McNeill, Terephthalate as a probe for photochemically generated hydroxyl radical, *J. Environ. Monit.*, 2010, **12**, 1658–1665.

45 K. S. W. Sing, Reporting physisorption data for gas/solid systems with special reference to the determination of surface area and porosity (Recommendations 1984), *Pure Appl. Chem.*, 1985, **57**, 603.

46 V. J. Keast, J. Ewald, K. S. B. De Silva, M. B. Cortie, B. Monnier, D. Cuskelly and E. H. Kisi, Optical properties and electronic structure of the Cu–Zn brasses, *J. Alloys Compd.*, 2015, **647**, 129–135.

47 I. I. Sasovskaya and V. P. Korabel, Optical properties of α- and β-CuZn brasses in the region of quantum absorption, *Phys. Status Solidi*, 1986, **134**, 621–630.

48 F. Ogata, H. Tominaga, H. Yabutani and N. Kawasaki, Removal of Estrogens from Water Using Activated Carbon and Ozone, *J. Oleo Sci.*, 2011, **60**, 609–611.

49 A. Zhang and Y. Li, Removal of phenolic endocrine disrupting compounds from waste activated sludge using UV, H_2O_2, and UV/H_2O_2 oxidation processes: effects of reaction conditions and sludge matrix, *Sci. Total Environ.*, 2014, **493**, 307–323.

50 T. W. Haas, *Kinetics of the uncatalyzed, alkaline decomposition of hydrogen peroxide*, 1960, p. 66.

51 P. Zhou, J. Zhang, Y. Zhang, J. Liang, Y. Liu, B. Liu and W. Zhang, Activation of hydrogen peroxide during the corrosion of nanoscale zero valent copper in acidic solution, *J. Mol. Catal. A: Chem.*, 2016, **424**, 115–120.

52 H. M. Coleman, V. Vimonses, G. Leslie and R. Amal, Removal of contaminants of concern in water using advance oxidation techniques, *Water Sci. Technol.*, 2007, **55**, 301–306.

53 E. Sarver, Y. Zhang and M. Edwards, Review of Brass Dezincification Corrosion in Potable Water Systems, *Corros. Rev.*, 2010, **28**, 155–196.

54 H. Lin and G. S. Frankel, Atmospheric corrosion of Cu by UV, ozone and NaCl, *Corros. Eng., Sci. Technol.*, 2013, **48**, 461–468.

55 X. Zhang, X. Liu, I. Odnevall Wallinder and C. Leygraf, The protective role of hydrozincite during initial corrosion of a Cu40Zn alloy in chloride-containing laboratory atmosphere, *Corros. Sci.*, 2016, **103**, 20–29.

56 P. A. Zhdan and J. E. Castle, Corrosion of brass in ultrapure water, *Surf. Interface Anal.*, 2002, **34**, 180–184.

57 S. Li and W. Sun, Photocatalytic degradation of 17α-ethinylestradiol in mono- and binary systems of fulvic acid and Fe(III): application of fluorescence excitation/emission matrixes, *Chem. Eng. J.*, 2014, **237**, 101–108.

58 I. M. Ramírez-Sánchez, S. Tuberty, M. Hambourger and E. R. Bandala, Resource efficiency analysis for photocatalytic degradation and mineralization of estriol using TiO_2 nanoparticles, *Chemosphere*, 2017, **184**, 1270–1285.

59 C.-H. Liao and M. D. Gurol, Chemical Oxidation by Photolytic Decomposition of Hydrogen Peroxide, *Environ. Sci. Technol.*, 1995, **29**, 3007–3014.

60 S. Luňák and P. Sedlák, Photoinitiated reactions of hydrogen peroxide in the liquid phase, *J. Photochem. Photobiol., A*, 1992, **68**, 1–33.

61 G. F. IJpelaar, D. J. H. Harmsen, E. F. Beerendonk, R. C. van Leerdam, D. H. Metz, A. H. Knol, A. Fulmer and S. Krijnen, Comparison of Low Pressure and Medium Pressure UV Lamps for UV/H_2O_2 Treatment of Natural Waters Containing Micro Pollutants, *Ozone: Sci. Eng.*, 2010, **32**, 329–337.

62 J. R. Bolton and M. I. Stefan, Fundamental photochemical approach to the concepts of fluence (UV dose) and electrical energy efficiency in photochemical degradation reactions, *Res. Chem. Intermed.*, 2002, **28**, 857–870.

63 D. B. Miklos, C. Remy, M. Jekel, K. G. Linden, J. E. Drewes and U. Hübner, Evaluation of advanced oxidation processes for water and wastewater treatment – a critical review, *Water Res.*, 2018, **139**, 118–131.

64 D. A. Devault, T. Néfau, Y. Levi and S. Karolak, The removal of illicit drugs and morphine in two waste water treatment plants (WWTPs) under tropical conditions, *Environ. Sci. Pollut. Res.*, 2017, **24**, 25645–25655.

65 Y. Valcárcel, F. Martínez, S. González-Alonso, Y. Segura, M. Catalá, R. Molina, J. C. Montero-Rubio, N. Mastroianni, M. López de Alda, C. Postigo and D. Barceló, Drugs of abuse in surface and tap waters of the Tagus River basin: heterogeneous photo-Fenton process is effective in their degradation, *Environ. Int.*, 2012, **41**, 35–43.

66 M. Catalá, N. Domínguez-Morueco, A. Migens, R. Molina, F. Martínez, Y. Valcárcel, N. Mastroianni, M. López de Alda, D. Barceló and Y. Segura, Elimination of drugs of abuse and their toxicity from natural waters by photo-Fenton treatment, *Sci. Total Environ.*, 2015, **520**, 198–205.

67 C. A. Martínez-Huitle, M. A. Quiroz, C. Comninellis, S. Ferro and A. De Battisti, Electrochemical incineration of chloranilic acid using Ti/IrO_2, Pb/PbO_2 and Si/BDD electrodes, *Electrochim. Acta*, 2004, **50**, 949–956.

68 W. Bors, C. Michel and M. Saran, On the nature of biochemically generated hydroxyl radicals. Studies using the bleaching of p-nitrosodimethylaniline as a direct assay method, *Eur. J. Biochem.*, 1979, **95**, 621–627.

69 N. N. Barashkov, D. Eisenberg, S. Eisenberg, G. S. Shegebaeva, I. S. Irgibaeva and I. I. Barashkova, Electrochemical chlorine-free AC disinfection of water contaminated with Salmonella typhimurium bacteria, *Russ. J. Electrochem.*, 2010, **46**, 306–311.

70 L. Zang, P. Qu, J. Zhao, T. Shen and H. Hidaka, Photocatalytic bleaching of p-nitrosodimethylaniline in TiO_2 aqueous suspensions: a kinetic treatment involving some primary events photoinduced on the particle surface, *J. Mol. Catal. A: Chem.*, 1997, **120**, 235–245.

71 A. B. R. Farhataziz, *Selected specific rates of reactions of transients from water in aqueous solutions III: hydroxyl radical and perhydroxyl radical and their radical ions*, Washington, 1977.

72 M. N. Desai and V. K. Shah, Aromatic amines as corrosion inhibitors for 70/30 brass in nitric acid, *Corros. Sci.*, 1972, **12**, 725–730.

73 G. C. Hobbs and J. Abbot, The Role of the Hydroxyl Radical in Peroxide Bleaching Processes, *J. Wood Chem. Technol.*, 1994, **14**, 195–225.

74 D. Yano, M. Murayama, M. Takahashi, H. Kobayashi and K. Yamanaka, Inhibition of Copper Corrosion by Removal of H_2O_2 From CO_2-Dissolved Water Using Palladium Catalysts, *ECS Trans.*, 2013, **58**, 151–158.

75 A. N. Pham, G. Xing, C. J. Miller and T. D. Waite, Fenton-like copper redox chemistry revisited: hydrogen peroxide and superoxide mediation of copper-catalyzed oxidant production, *J. Catal.*, 2013, **301**, 54–64.

76 L. C. Friedrich, M. A. Mendes, V. O. Silva, C. L. P. S. Zanta, A. Machulek Jr and F. H. Quina, Mechanistic implications of zinc(II) ions on the degradation of phenol by the Fenton reaction, *J. Braz. Chem. Soc.*, 2012, **23**, 1372–1377.

77 T. Ozawa and A. Hanaki, The first ESR spin-trapping evidence for the formation of hydroxyl radical from the reaction of copper(II) complex with hydrogen peroxide in aqueous solution, *J. Chem. Soc., Chem. Commun.*, 1991, 330–332.

78 J. K. Kim and I. S. Metcalfe, Investigation of the generation of hydroxyl radicals and their oxidative role in the presence of heterogeneous copper catalysts, *Chemosphere*, 2007, **69**, 689–696.

79 P. Qiu and C. Leygraf, Initial oxidation of brass induced by humidified air, *Appl. Surf. Sci.*, 2011, **258**, 1235–1241.

80 R. Yatskiv, S. Tiagulskyi, J. Grym, J. Vaniš, N. Bašinová, P. Horak, A. Torrisi, G. Ceccio, J. Vacik and M. Vrňata,

Optical and electrical characterization of CuO/ZnO heterojunctions, *Thin Solid Films*, 2020, **693**, 137656.

81 P. Nandi and D. Das, ZnO-Cu_xO heterostructure photocatalyst for efficient dye degradation, *J. Phys. Chem. Solids*, 2020, **143**, 109463.

82 V. Augugliaro, V. Loddo, M. Pagliaro, G. Palmisano and L. Palmisano, *Clean by Light Irradiation: Practical Applications of Supported TiO_2*, RSC Publishing, Cambridge, UK, 2010.

83 P. Zhou, An in situ kinetic investigation of the selective dissolution mechanism of Cu alloys, PhD thesis, Pierre and Marie Curie University, 2017, 181.

84 L. Burzyńska, Comparison of the spontaneous and anodic processes during dissolution of brass, *Corros. Sci.*, 2001, **43**, 1053–1069.

85 O. Kozaderov, K. Shikhaliev, C. Prabhakar, A. Tripathi, D. Shevtsov, A. Kruzhilin, E. Komarova, A. Potapov, I. Zartsyn and Y. Kuznetsov, Corrosion of α-Brass in Solutions Containing Chloride Ions and 3-Mercaptoalkyl-5-amino-1H-1,2,4-triazoles, *Appl. Sci.*, 2019, **9**, 2821.

86 M. C. Bastos, L. F. A. Proença, M. M. M. Neto and I. T. E. Fonseca, Electrochemical studies on the corrosion of brass in seawater under anaerobic conditions, *J. Solid State Electrochem.*, 2008, **12**, 121–131.

87 D. P. Whittle and G. C. Wood, The Establishment and Growth of Zinc Oxide on 74:26 Brass, *Br. Corros. J.*, 1968, **3**, 294–300.

88 G. Hultquist, P. Szakálos, M. J. Graham, A. B. Belonoshko, G. I. Sproule, L. Gråsjö, P. Dorogokupets, B. Danilov, T. AAstrup, G. Wikmark, G.-K. Chuah, J.-C. Eriksson and A. Rosengren, Water Corrodes Copper, *Catal. Lett.*, 2009, **132**, 311–316.

89 E. A. Thompson and T. D. Burleigh, Accelerated corrosion of zinc alloys exposed to ultraviolet light, *Corros. Eng., Sci. Technol.*, 2007, **42**, 237–241.

90 M. Li, Z. Wang, Q. Zhang, C. Qin, A. Inoue and W. Guo, Formation and evolution of ultrathin Cu_2O nanowires on NPC ribbon by anodizing for photocatalytic degradation, *Appl. Surf. Sci.*, 2020, **506**, 144819.

91 B. Y. Valles-Pérez, M. A. Badillo-Ávila, G. Torres-Delgado, R. Castanedo-Pérez and O. Zelaya-Ángel, Photocatalytic activity of ZnO + CuO thin films deposited by dip coating: coupling effect between oxides, *J. Sol-Gel Sci. Technol.*, 2020, **93**, 517–526.

92 H. Yoo, S. Kahng and J. Hyeun Kim, Z-scheme assisted ZnO/Cu_2O-CuO photocatalysts to increase photoactive electrons in hydrogen evolution by water splitting, *Sol. Energy Mater. Sol. Cells*, 2020, **204**, 110211.